AIAA JOURNAL
Vol. 48, No. 12, December 2010

Supersonic Drag Reduction with Repetitive Laser Pulses Through a Blunt Body

Akihiro Sasoh,* Yohei Sekiya,† Takeharu Sakai,‡ Jae-Hyung Kim,§ and Atsushi Matsuda¶
Nagoya University, Nagoya 464-8603, Japan

DOI: 10.2514/1.J050174

The drag over a 20-mm-diam, flat-nosed cylinder with repetitive laser pulse irradiations ahead of it was experimentally measured in a Mach-1.92, in-draft wind tunnel. Ten-ns laser pulses (wavelength, 1047 nm) were focused using a plane-convex lens fabricated on the nose of the cylinder at a repetition frequency of up to 10 kHz and power of 70 W at a maximum. The steady-state drag was measured using a low-friction piston, which was backed by a load cell in a cavity at a controlled pressure. Within the limited laser performance, 3% drag decrease and efficiency of energy deposition of up to 10 were obtained on a time-averaged basis. The stronger the interactions between the laser-heated gas and the bow shock wave, the larger the amount of drag reduction became, however, with degraded performance of laser power transmission to the flow.

Nomenclature

A = cross-sectional area of cylinder model
c = constant
D = drag
D_B = drag without energy deposition
D_W = drag with energy depositions
E = laser energy per pulse output from device
E_{eff} = laser energy per pulse effectively input in flow
F_L = force from load cell to cylinder model, positive left
F_O = resultant force from O-rings to cylinder model, positive right
f = laser pulse repetition frequency
l = distance between cylinder nose and laser focus
P = static pressure
P_0 = atmospheric pressure
P_{sub} = static pressure in subchamber
t = time originated in (first) laser pulse irradiation
U = test flow speed
V = output voltage of load cell
V_B = output voltage of load cell during wind tunnel run without laser energy deposition
V_W = output voltage of load cell during wind tunnel run with laser energy depositions
W = time-averaged laser power $= fE$
α = constant determined in calibration
β = constant determined in calibration
ΔD = decrement in drag due to energy depositions
η = efficiency of energy deposition

Presented as Paper 2009-3585 at the 40th AIAA Plasmadynamics and Lasers Conference, San Antonio, TX, 22–25 June 2009; received 2 September 2009; revision received 25 May 2010; accepted for publication 31 August 2010.

*Professor, Department of Aerospace Engineering, Furo-cho, Chikusa-ku. Associate Fellow AIAA.
†Graduate Student, Department of Aerospace Engineering, Furo-cho, Chikusa-ku; currently Engineer, All Nippon Airways, Shiodome-City Center, 1-5-2, Higashi-Shimbashi, Minato-ku, Tokyo 105, Japan.
‡Associate Professor, Department of Aerospace Engineering, Furo-cho, Chikusa-ku. Member AIAA.
§Graduate Student, Department of Aerospace Engineering, Furo-cho, Chikusa-ku.
¶Research Associate, Department of Aerospace Engineering, Furo-cho, Chikusa-ku; Currently Assistant Professor, Department of Mechanical Engineering, Meijo University, 1-501 Shiogamaguchi, Tenpaku-ku, Nagoya 468, Japan. Member AIAA.

I. Introduction

AT THE present state of the art, realizing economic supersonic flight is hampered by poor aerodynamic performance due to wave drag. The magnitude of the wave drag strongly depends on the shape of the vehicle. As was reviewed in [1], various low-wave-drag schemes, including a solid spike attached to a nose of the body, the injection of cold or hot jet from the nose, were examined. More recently, it was demonstrated that further aerodynamic performance modification was possible by depositing a power ahead of a body. This scheme, so-called energy deposition, has collected strong attention, and related investigations have been much conducted [2–12].

Knight [2] characterizes the energy deposition scheme by using a deposited energy, pulse duration and pulse interval in respective dimensionless forms. If the pulse interval is long enough, flow after a pulse energy deposition is independent from previous pulses. Adelgren et al. [7] conducted experimental study of a single laser pulse energy deposition over a sphere in a supersonic flow with Mach number of 3.45. The flow was visualized by schlieren method and local pressure histories were measured using a piezo-resistive pressure transducer that was recess mounted in the sphere model. An energy was deposited using an Nd:YAG laser pulse (wave length, 532 nm; pulse duration, 10 ns; pulse energy, 12 to 300 mJ). Kandala and Candler [11] and Zheltovodov et al. [12] conducted numerical simulation of Adelgren et al.'s experiment, thereby reproducing basic characteristics of the pressure modulation at the stagnation point. Sakai et al. [10] conducted a similar experiment in an in-draft wind tunnel with Mach number of 3.0, and measured the stagnation pressure history using a flush-mounted piezoelectric pressure transducer, which was reproduced in their own numerical simulation.

Tret'yakov et al. [13] conducted steady-state drag measurement in Mach-2 argon flow by irradiating CO_2 laser pulses at a repetition frequency of up to 100 kHz. A significant drag reduction of up to 45% of the baseline drag was obtained. However, as well as the amount of drag reduction itself, there is another important criterion in the drag reduction performance with energy depositions, that is the efficiency of energy deposition, η, defined in [2]:

$$\eta = \frac{U\Delta D}{fE} \tag{1}$$

The numerator on the right-hand side in Eq. (1) equals the propulsion power saved due to energy depositions, the denominator the time-averaged power of energy depositions. In order for the energy

deposition scheme to be practically useful, η needs to be larger than unity. In [13], however, operation data with η being larger than unity was not presented.

With a blunt nose such as a sphere and flat-nose cylinder the amount of drag reduction is significant although the baseline drag, that is the one without energy deposition, is large. On the other hand, a sharp nose like a cone has a small baseline drag, yet the impact of energy depositions is small because the residence time of the modulated flow due to energy deposition is shorter. To obtain good tradeoff between the baseline drag and the impact of energy depositions, Sakai [14] proposed a truncated cone with energy pulse depositions. In his numerical simulation, condition that the drag becomes smaller than that of a conical nose of the same apex angle and that the efficiency of energy deposition exceeds unity were both satisfied. This promising result strongly encourages further studies of this subject.

One of the key issues is to accurately measure the drag reduction due to energy depositions. Surface pressure measurement on the body using pressure transducers has modest spatial resolution; the momentum modulation which is measured by spatiotemporally integrating the pressure also has modest accuracy. Moreover, if energy deposition repetition frequency is high, the drag performance and associated flow are influenced by preceding pulses so that the preceding-mentioned single-pulse performance evaluation does not reflect those of repetitive-pulse operation. If a large wind tunnel is available for the present purpose, we can use a force balance presumably installed in the facility. However, usually this kind of large facility is shared by many other users so that arrangement for energy pulse depositions is not readily done within a given turnaround period and flexibility. It is difficult to accurately predict the amount of drag reduction only by numerical simulation because the amount of laser energy effectively deposited into the flow depends strongly on experimental setup conditions. This study aims in measuring time-averaged drag reduction performance that is modulated with repetitive laser pulse energy depositions up to 10 kHz, and to quantitatively analyze associated drag reduction mechanisms through experimental and numerical diagnostics.

II. Apparatus and Methods

A. Wind Tunnel

Figure 1 shows a schematic illustration of the experimental setup developed in this study. It comprises an in-draft wind tunnel, a repetitive-pulse Nd:YLF (neodymium: yttrium lithium fluoride) laser, a test model with a drag measurement device, diagnostic system including schlieren optics. The supersonic nozzle is designed for a flow Mach number of 2.0 using a method of characteristics. Then, the correction against a boundary layer is done through numerical simulation. From a pitot pressure of 72.2 kPa at the centerline of the freestream and a static pressure of 13.8 kPa on the side wall at the test model nose location, which are measured under a typical operation condition, the test flow Mach number is evaluated to be 1.92 from Rayleigh–pitot formulas. In the projection area of the cylinder model of a diameter of 20 mm, the Mach number has a maximum deviation of ± 0.005. The wind tunnel test section has an 80×80 mm square cross section. The frames of the wind tunnel are made of brass; the windows of acrylic. The intake of the wind tunnel is made of brass, and has a 440×440 mm square inlet cross section. The nozzle, made of aluminum, is connected to a vacuum chamber with an inner volume of 11.5 m^3. Between the nozzle and the vacuum chamber, a pneumatic butterfly valve is installed. Right downstream of the test section, the flow passage is enlarged so that instruments can fit to the limited test section volume. The available test time of the wind tunnel is about 10 s.

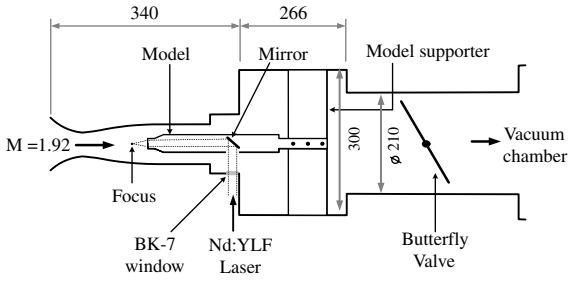

Fig. 1 Experimental setup (cross-sectional side view), length in mm.

B. Method of Drag Measurement

In the test section, a 20-mm-diam cylinder model is placed with a housing that is designed for the drag measurement (see Fig. 2). The cylinder model is held in the housing using two O-rings. The clearance between the cylinder model and the housing is set to the order of 500 μm. In the room of the housing behind the cylinder model, a load cell (MR-50N-0418, Showa Measurement Instrument Co., maximum load 50 N) is fabricated so that the force balance over the cylinder model is measured. The room is pneumatically isolated from the wind tunnel test section, and is connected to a subchamber (inner volume; 0.018 m^3) outside of the wind tunnel. The pressure in the subchamber, P_{sub}, is regulated and monitored using a semiconductor pressure transducer (DG-920, Tokyo Aircraft Instrument Co.).

The following axial force balance over the cylinder model holds:

$$D - AP_{\text{sub}} + F_O - F_L = 0 \tag{2}$$

where the first term on the left-hand side corresponds to a force exerting on the model head immersed in the test flow, which is of the primary interest in this study as the drag; the second term to a pneumatic force exerting on the model tail in the housing; third to a resultant force from the O-rings; the forth to a force from the load cell. Note here that F_O cannot be designed a priori, but should be measured in in situ calibration. In theory, the reaction force of F_O to the O-rings should be balanced with pneumatic forces due to the pressure difference across an O-ring and the friction forces at the interface between an O-ring and the housing inner wall. It is practically difficult to evaluate the respective contributions. Yet, in the following procedure, we can calibrate the force balance system without quantifying each of them. Considering the preceding-mentioned force balance on the O-rings, F_O is approximated by the following equation:

$$F_O = c_1(D - AP_{\text{sub}}) + c_2 \tag{3}$$

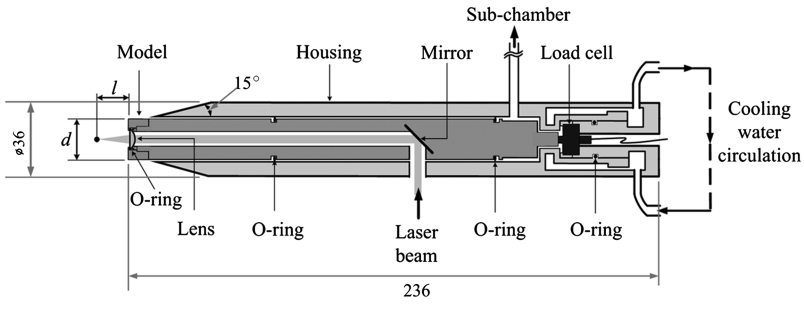

Fig. 2 Schematic illustration of piston-type force balance system, length in mm.

Substituting Eq. (3) into Eq. (2) yields

$$F_L = (1 + c_1)(D - AP_{\text{sub}}) + c_2 \tag{4}$$

The output signal of the load cell scales with F_L:

$$F_L = c_3 V \tag{5}$$

where c_3 is the nominal sensitivity of the load cell. Combining Eqs. (4) and (5),

$$V = \frac{1 + c_1}{c_3}(D - AP_{\text{sub}}) + \frac{c_2}{c_3} \equiv \alpha(D - AP_{\text{sub}}) + \beta \tag{6}$$

where α and β are constants which should be determined from calibration.

To calibrate the force balance system, in each series of experiments we conduct in situ static calibration before and after a series of experiments of a day. The force balance system of Fig. 2 is set in the quiescent atmosphere. In this case,

$$D = AP_0 \tag{7}$$

A force balance is controlled by varying P_{sub}. In Fig. 3, the circled labels correspond to the sequential number of the calibration processes, and are also used as a subscript. First, at the atmospheric pressure, $P_0 = 101$ kPa, the model is inserted into the housing (state 0). Then P_{sub} is decreased from about P_0 to $P_{\text{sub},1} = 30$ kPa (state 1). At this moment, because the pressure difference between the head and tail of the cylinder model has a maximum value, a maximum force is exerted on to the load cell. Thereafter, P_{sub} is increased step by step. The load cell output signal, V, and the pressure difference $P_0 - P_{\text{sub}}$ exhibited linear dependence with a sufficient response time of shorter than 0.1 s down to $P_0 - P_{\text{sub}} = 10$ kPa (state 7). Further decrease in the pressure difference results in deviation from the linear dependence (states 8 and 9). In this calibration, a linear relation of Eq. (6), and then the values of α and β can be obtained in the range between the states 1 and 7.

Before a wind tunnel run, P_{sub} is set from the atmospheric (P_0) to an appropriately-lower value, for example, $P_{\text{sub},2} \cong 40$ kPa. Next, it is increased by about 10 kPa ($P_{\text{sub},3} \cong 50$ kPa), and then is kept constant during the wind tunnel run. The force balance before wind tunnel run is given from Eqs. (6) and (7):

$$V_3 = \alpha A(P_0 - P_{\text{sub},3}) + \beta \tag{8}$$

After starting the wind tunnel run, the pressure difference becomes further decreased because of a total pressure loss in the shock layer over the cylinder model head. However, it should be within the linear range. From Eq. (6) the output signal with the wind tunnel run but without laser energy depositions, V_B, which corresponds to a baseline drag of D_B, is given by

$$V_B = \alpha(D_B - AP_{\text{sub},3}) + \beta \tag{9}$$

The drag without energy depositions, D_B, is obtained by subtracting Eqs. (8) from (9):

$$D_B = AP_0 - \frac{V_3 - V_B}{\alpha} \tag{10}$$

Note here that Eq. (10) does not contain β which has a large run-to-run uncertainty. Since the uncertainty in α is much smaller, within 1.7%, D is obtained with this high accuracy. In the same way, the decrement in the drag due to energy depositions, ΔD, is determined from the output signal that is obtained with laser energy depositions, V_W, by

$$\Delta D = D_B - D_W = \frac{V_B - V_W}{\alpha} \equiv \frac{\Delta V}{\alpha} \tag{11}$$

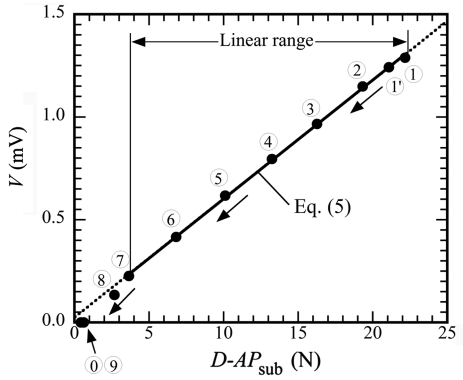

a) Calibration line

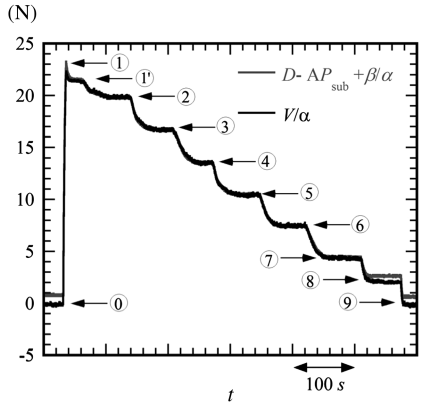

b) Time variations of pressure difference and load cell signal, $D = AP_0$, $P_0 = 101$kPa

Fig. 3 Example of in situ calibration of force balance system.

C. Laser and Optics

A highly-repetitive, Nd:YLF laser [wavelength, 1047 nm; pulse duration, 10 ns (full width at half-maximum); repetition frequency, 10 kHz maximum; average power, 80 W maximum] is used for energy depositions. The output laser beam with a 5×5 mm square cross section, is reflected against three 45 deg reflection mirrors for 1-μm wavelength light before the wind tunnel, then sent through a BK-7 window to the test section in the wind tunnel. Inside the cylinder model (see Fig. 2), the laser beam is reflected on another 45 deg mirror and is transmitted through a plane-convex mirror with a focus length of 10 to 30 mm. In this optical arrangement, any mechanics does not disturb the test flow. The time-averaged laser power is measured using a power meter (F150A, Ophir) behind the BK-7 window. From measurement of the temporal laser power history using a photodiode, it turns out that a laser energy per pulse has a shot-to-shot scatter within a factor of about $\pm 20\%$. This issue is carefully taken into consideration in the following analyses and discussions.

D. Diagnostics

Framing schlieren visualization is done using a high-speed framing camera (HPV-1, Shimadzu Co., 312×260 pixels, 10^6 frame/s maximum, 100 frames). A xenon flush lamp (SA-200F, Nissin Electronic Co., duration, 2 ms) is used as the light source. A pair of 300-mm-diam concave mirrors (focal lengths, 1 and 2 m) are used to obtain and image a collimated beam for the flow visualization through the test section. The output signals of the load cell, static pressure in the test section, the pressure in the subchamber and laser pulse irradiations are recorded in a digital storage scope (DL750, Yokogawa Co.).

E. Numerical Simulation

A computational fluid dynamic (CFD) method is used to simulate the experimental conditions. A two-dimensional axisymmetric flowfield over the flat-nosed cylinder is assumed to be inviscid. A specific heat ratio is taken to be a constant value of 1.4. The advection upstream splitting method flux difference and flux vector scheme is

used to evaluate the numerical flux functions. The mass, momentum, and energy conservation equations are integrated with a constant time step of 3 ns using a second-order Runge–Kutta method. When calculations were performed with the step size of 1 ns, there was no discernible difference between the two calculated results. Therefore, the time step size used was believed to be adequately small to simulate the experimental conditions considered in the present study. Computed flow properties are second-order accurate in space. A heating source term for a periodic laser energy deposition is included in the energy equation: the laser energy is deposited during the period of the laser pulse duration at constant volume assuming that the deposited region is spherically symmetric and that the spatial distribution within the deposited region is given as a Gaussian profile [12,14].

The effectively-input energy value to the flow needs to be specified for calculation: a nominal value of 45% of the laser output energy is selected by fitting the calculated result to the experimental blast wave evolution. The effect of the effectively-input energy on the obtained drag reduction will be examined in the next section. A set of the freestream properties are taken from a typical wind tunnel operating

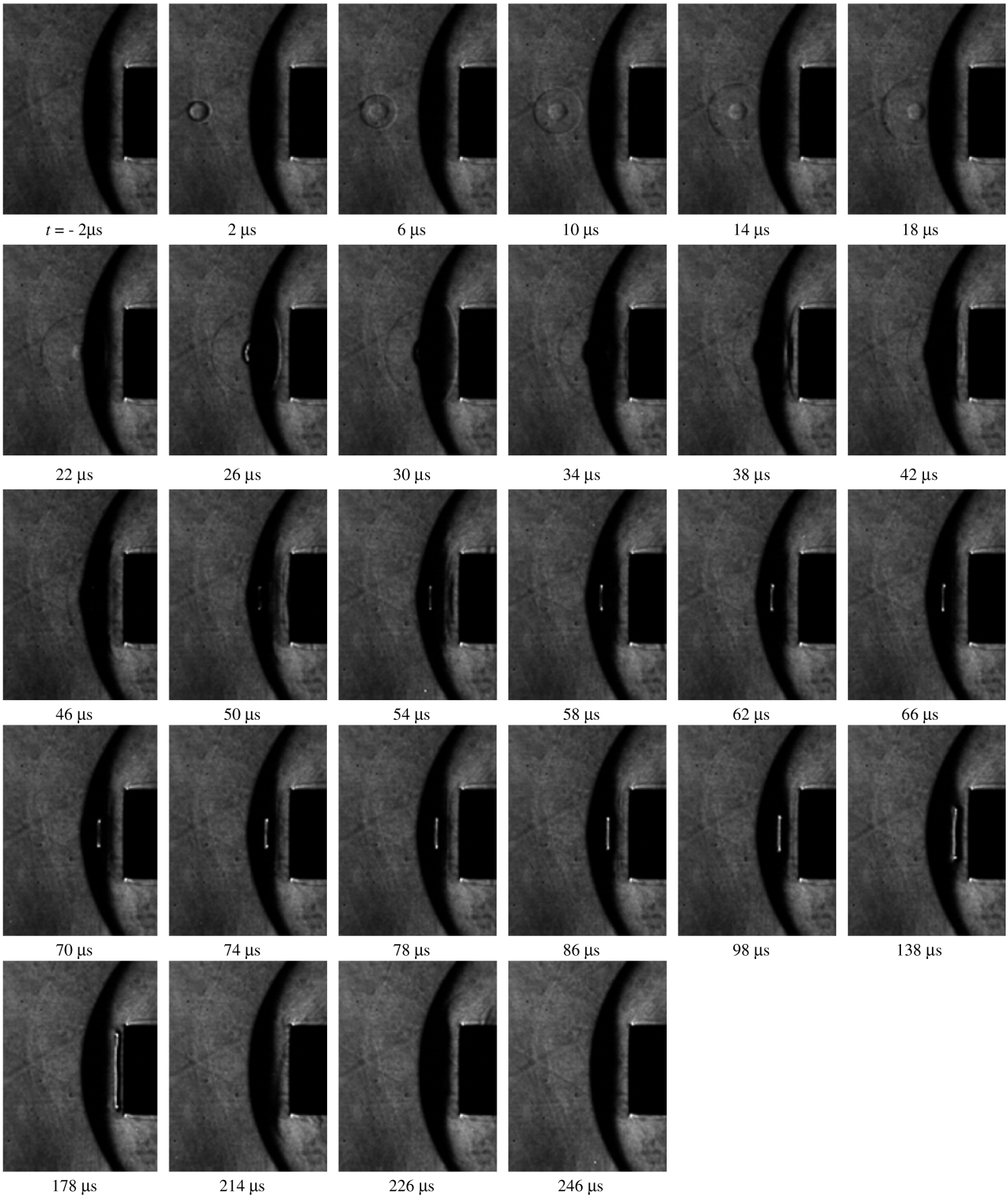

Fig. 4 Framing schlieren images with single-pulse irradiation, $l/d = 1.06$, $E = 12.0$ mJ, framing interval $= 4$ μs, exposure $= 0.5$ μs, t is originated in the moment of laser pulse irradiation.

condition: static pressure and temperature and Mach number are set to 13.8 kPa, 163 K, and 1.92, respectively. A slip condition is imposed at a wall of the flat-nosed body. All calculated values are given by using 201×301 computational grids. The number of grids used is believed to be sufficient for the present purpose; the drag value obtained by using 201×401 grids for a blunt body differed only by about 1% compared with the one by using 201×201 grids [14].

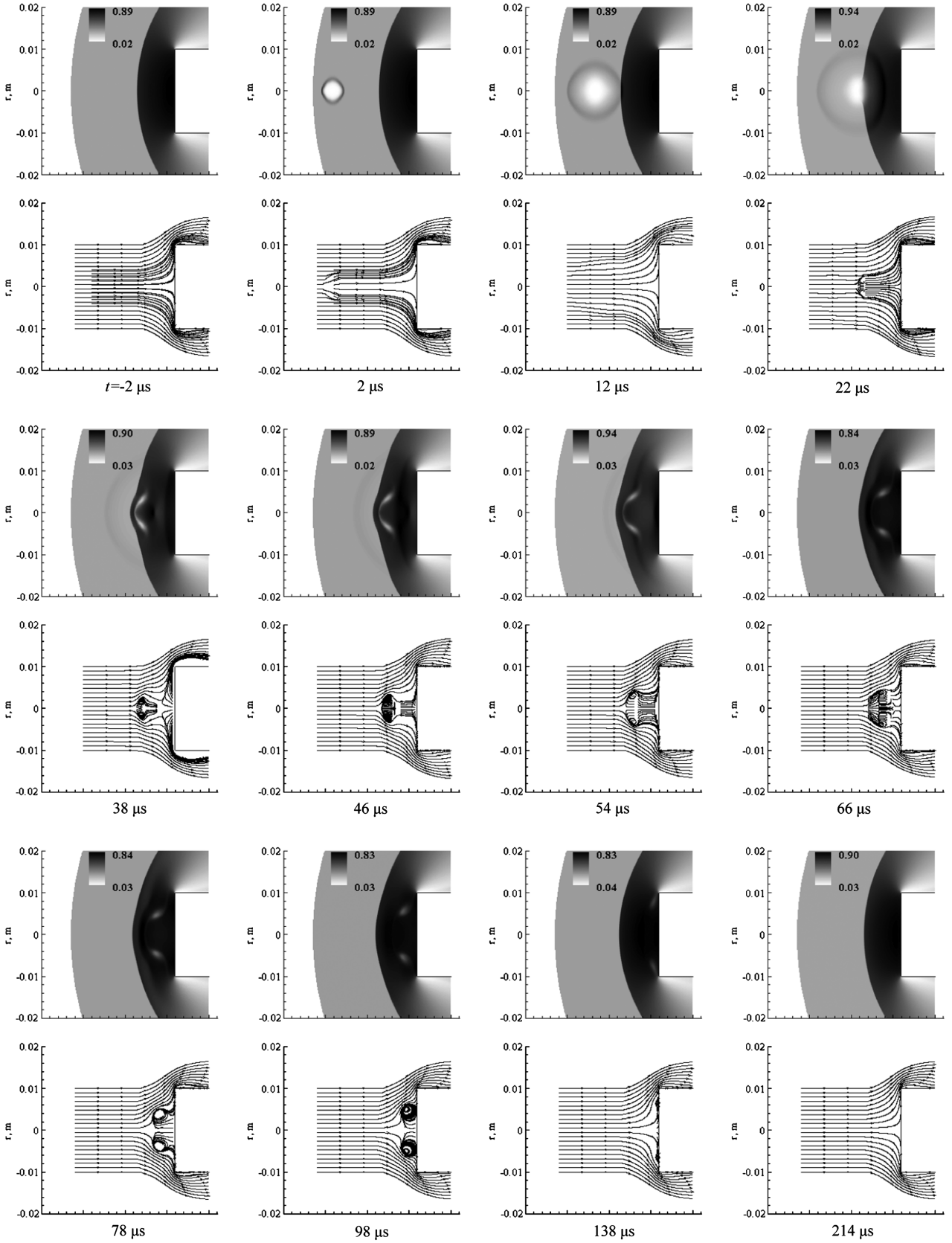

Fig. 5 Numerical isopycnics (upper) and temporal streamlines (lower) under the same operation conditions as of Fig. 4, the number below each plot corresponds to the time synchronized to that of Fig. 4. The effectively-input energy to the flow is assumed to be 45% of the laser output energy, that is $E_{\mathrm{eff}} = 5.4\ \mathrm{mJ/pulse} = 0.45E$.

III. Flow Visualization

Figure 4 shows framing schlieren images after the first laser pulse. The time origin, $t = 0$, is set to the moment of the laser pulse irradiation. A trigger signal is sent to control the high-speed camera precedence of the laser irradiation. At $t = -2$ μs, the test flow has not experienced the laser pulse irradiation. In the steady-state supersonic flow, a standing bow shock wave is formed over the cylinder. After the laser pulse is irradiated, a laser-heated gas is formed and expands through optical breakdown, forming a spherical, low-density region upstream of the bow shock. It drives a laser-induced blast wave that propagates ahead of the laser-heated gas. Because of convection, they approach the bow shock wave. At $t = 14$ μs, the laser-induced shock wave on the downstream side has already entered the shock layer. At $t = 22$ μs, the laser-heated gas has entered the shock layer. During $t = 26$ μs to 46 μs, due to the "lens effect" [2,7] the bow shock wave around the center axis extrudes upstream. At $t = 50$ μs and thereafter, the laser-heated gas is recognized as a torus that has a bright contrast in the dark shock layer. During its convection, it is radially stretched, thereby reaching the full diameter of the model nose. At $t = 214$ μs and thereafter, the laser-heated gas leaves past the peripheral of the flat nose. At $t = 246$ μs, the flow has almost restored to the initial steady state.

Figure 5 shows numerical simulation results corresponding to the same operation conditions as of Fig. 4. It is assumed that 45% of the laser output energy is effectively input to the flow. At $t = 2$ μs, a new laser-heated gas sphere is formed upstream of the model. The flow incident on the sphere is deflected around. At $t = 12$ μs, the laser-induced shock wave has penetrated in the bow shock layer. The laser-heated gas barely stays upstream of it. At $t = 22$ μs, a toroidal vortex starts to be formed due to the baroclinic interaction between the bow shock layer and the laser-heated gas sphere [2,5,15]. During $t = 38$ and 66 μs, the laser-heated gas is penetrated into the shock layer, and its original spherical structure is deformed; the bow shock wave near the centerline extrudes and slowly recovers its original shape; and the vortex torus is stretched radially during its convection. During $t = 78$ and 138 μs, the vortex torus still stays over the nose, thereby the pressure on the nose remaining reduced. At $t = 214$ μs, the influence of the laser pulse almost diminished.

IV. Drag Reduction Characteristics

Figure 6a shows the example of an experimentally-measured history of a drag that is normalized by the baseline value, D_B, that is without laser pulse irradiation. The 1-s duration of the laser pulse irradiations is indicated by an arrow labeled *Laser ON*. Before and after the laser pulse irradiations, the drag exhibits a steady-state value with fluctuation of a root mean square (rms) of 0.9%. During the laser pulse irradiations, the drag is decreased by about 3%, which is 3.3 times larger than the rms of the fluctuation. In the figure, the normalized drag that is obtained by numerical simulation under the corresponding operation conditions is also plotted with the same time resolution as of the experiment, which is 0.5 ms. In the numerical simulation, the effectively-input laser energy into the flow, E_{eff}, is assumed to equal to 45% of the laser output energy, E, as is in the case of Fig. 5. Figure 6b shows the same numerical drag history plotted with the real time resolution in the numerical simulation of 3 ns. After a laser pulse deposition, the drag experiences a spiky increase that is caused by the reflection of the blast wave, then decreases due to the expansion waves propagating in the shock layer that is generated by the interaction with the laser-heated gas. The drag once restores and then experiences a much longer decrease which lasts about 120 μs. After the interval to the next laser pulse, 250 μs, the interaction becomes much weaker and the drag almost restores. This cycle continues with successive energy depositions. The time-averaged drag is decreased by 3.2% of the baseline drag.

Figure 7a shows drag reduction performance with varying laser power, $W = fE$. In the experiments (EXP), three values of E are examined although available range of f-E combination is quite limited. Within the experimentally available laser operation conditions, an up-to-3% drag reduction is realized. Corresponding

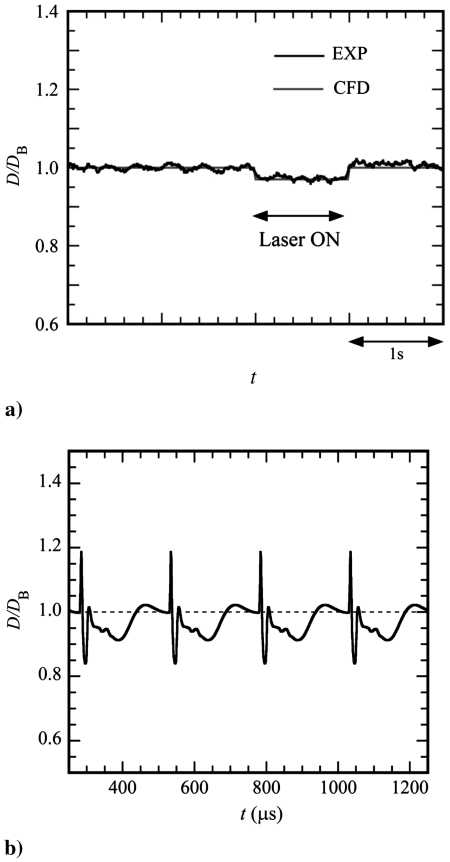

Fig. 6 Normalized drag histories, $l/d = 1.06$, $f = 4$ kHz, $E = 12.0$ mJ/pulse, $W = 47.8$ W; EXP, experiment, $D_B = 22.4 \pm 0.3$ N; CFD, numerical simulation, $D_B = 20.6$ N, $E_{\text{eff}}/E = 0.45$: a) experimental time resolution of 0.5 ms and b) time resolution of 3 ns, CFD.

performance obtained in the numerical simulation (CFD) is also plotted. In CFD, three values of E_{eff}/E, 0.30, 0.45 and 0.60, are examined. Since in the present case $E_{\text{eff}}/E = 0.45$ best fits to the experimental performance, this value is regarded as the nominal value in CFD. However, the effective value of the ratio strongly depends on the experimental conditions.

In CFD, the normalized drag reduction performance with a constant value of E_{eff}/E depends primarily on W. The EXP performance follows this tendency except for the highest power range of about 70 W. Figure 7b plots the experimental and numerical performance of the efficiency of energy deposition, η. In EXP, an efficiency of up to 10 is obtained at the lowest power of 28 W. Then the efficiency monotonically decreases with increasing W. On the other hand, in CFD, η with $E_{\text{eff}}/E = 0.45$ equals 6.8 at 28 W then stays an almost constant value of 6.3 ± 0.1 in the range of 40 to 70 W. In CFD, the interaction between successive energy depositions is weak; the drag modulation repeats almost the same history from the beginning of the simulation. However, the experimental performance suggests that the experimentally-effective value of E_{eff}/E seems to decrease with increasing W. Moreover, this degradation becomes more significant when a smaller energy is irradiated with a higher repetition frequency. η with $E = 7.0$ mJ at $f = 10$ kHz (71.5 W) is smaller than that with $E = 8.6$ mJ at $f = 8$ kHz (69 W) by more than one on average. This difference seems to have physical significance; with energy depositions the flow field in the shock layer does not completely recover to the initial steady state: the optical performance for the laser power transmission of the shock layer should be degraded due to the fluctuated density field with increasing the laser power; the value of E_{eff} should be decreased. This problem is caused by the present optical path for laser pulse transmission from the head of the model through the shock layer. The more the shock layer is disturbed by the energy depositions, the more serious the influence to

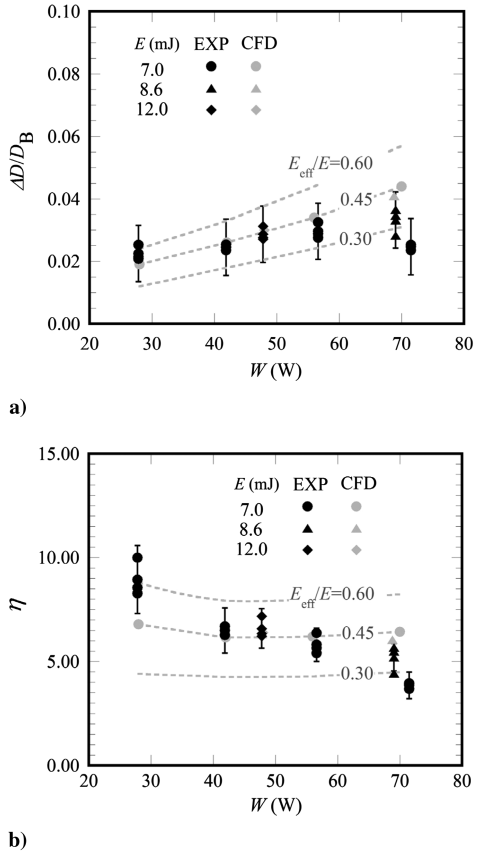

Fig. 7 Drag reduction performance with respect to laser power, $l/d = 1.06$; EXP, experiment; CFD, numerical simulation with three values of E_{eff}/E, the experimental E has a scatter of ± 0.2 J/pulse: a) normalized drag reduction and (b) efficiency of energy deposition. The largest error is caused by drag fluctuation in the experiment; the error bars correspond to the rms of the drag fluctuation.

the laser beam optics. To solve this problem, the laser beam path needs to be modified, which is beyond the scope of the present study.

V. Conclusions

In this study, we have developed an experimental system to examine steady-state drag reduction performance with repetitive laser pulse irradiations; the drag was measured from a force balance over the backpressure-controlled piston using a load cell; repetitive laser pulses of up to 10 kHz were sent through the nose of the cylinder model. Within the limited laser power capability, we have experimentally demonstrated time-averaged drag reduction performance, 3% drag decrease and efficiency of energy deposition up to 10. The numerical simulation well diagnoses the drag reduction mechanisms, in which baroclinic vortex generation caused by interactions between the laser-heated gas and the bow shock layer plays an important role. In the present onboard laser optics, the disturbed shock layer degrades the effective laser power transmission performance at a high repetition frequency of around 10 kHz. According to Sakai [14], a much higher drag reduction performance is expected at an even higher repetition frequency of 50 kHz and higher. A clear target of the next step is to improve the laser pulse transmission optics so that laser energy depositions remain efficient in an even higher repetition frequency range.

Acknowledgments

This research was supported by Japan Society for Promotion of Science as Grant-in-Aid for Scientific Research, No. 19206089. The authors would like to express their gratitude to A. Saito and K. Kumazawa, Technical Division, Nagoya University, for their valuable technical assistance.

References

[1] Bushnell, D. M., "Shock Wave Drag Reduction," *Annual Review of Fluid Mechanics*, Vol. 36, 2004, pp. 81–96. doi:10.1146/annurev.fluid.36.050802.122110

[2] Knight, D., "Survey of Aerodynamic Drag Reduction at High Speed By Energy Deposition," *Journal of Propulsion and Power*, Vol. 24, No. 6, 2008, pp. 1153–1167. doi:10.2514/1.24595

[3] Riggins, D., Nelson, H. F., and Johnson, E., "Blunt-Body Wave Drag Reduction Using Focused Energy Deposition," *AIAA Journal*, Vol. 37, No. 4, 1999, pp. 460–467. doi:10.2514/2.756

[4] Kremeyer, K., Sebastian, K., and Shu, C. W., "Computational Study of Shock Mitigation and Drag Reduction by Pulsed Energy Lines," *AIAA Journal*, Vol. 44, No. 8, 2006, pp. 1720–1730. doi:10.2514/1.17854

[5] Taguchi, S., Ohnishi, N., Furudate, M., and Sawada, K., "Numerical Analysis of Drag Reduction for Supersonic Blunt Body by Pulse Energy Deposition," AIAA Paper 2007-1235, Jan. 2007.

[6] Georgievskii, P., and Levin, V., "Bow Shock Wave Structures Control by Pulse-Periodic Energy Input," AIAA Paper 2004-1019, 2004.

[7] Adelgren, R. A., Yan, H., Elliott, G. S., Knight, D. D., Beutner, T. J., and Zheltovodov, A. A., "Control of Edney 4 Interaction by Pulsed Laser Energy Deposition," *AIAA Journal*, Vol. 43, No. 2, 2005, pp. 256–269. doi:10.2514/1.7036

[8] Georgievsky, P., and Levin, V., "Unsteady Interaction of a Sphere with Atmospheric Temperature Inhomogeneity at Supersonic Speed," *Mekhanika Zhidkosti i Gaza*, Vol. 4, No. 4, May–June 1993, pp. 174–183 (in Russian); translated in *Fluid Dynamics*, Vol. 28, No. 4, 1993, pp. 568–574. doi:10.1007/BF01342694

[9] Borzov, V. Y., Rybka, I. V., and Yur'ev, A. S., "Effect of Local Energy Supply to a Hypersonic Flow on the Drag of Bodies with Different Nose Bluntness," *Journal of Engineering Physics and Thermophysics*, Vol. 67, Nos. 5–6, 1995, pp. 997–1002. doi:10.1007/BF00852714

[10] Sakai, T., Sekiya, Y., Mori, K., and Sasoh, A., "Interaction Between Laser-Induced Plasma and Shock Wave over a Blunt Body in a Supersonic Flow," *Proceedings of the Institution of Mechanical Engineers. Part G, Journal of Aerospace Engineering*, Vol. 222, No. 5, 2008, pp. 605–617. doi:10.1243/09544100JAERO294

[11] Kandala, R., and Candler, G. V., "Numerical Studies of Laser Induced Energy Deposition for Supersonic Flow Control," *AIAA Journal*, Vol. 42, No. 11, 2004, pp. 2266–2275. doi:10.2514/1.6817

[12] Zheltovodov, A. A., Pimonov, E. A., and Knight, D. D., "Energy Deposition Influence on Supersonic Flow over Axisymmetric Bodies," AIAA Paper 2007-1230, Jan. 2007.

[13] Tret'yakov, P. K., Garanin, A. F., Grachev, G. N., Krainev, V. L., Ponomarenko, A. G., Tishchenko, V. N., and Yakovlev, V. I., "Control of Supersonic Flow Around Bodies by Means of High-Power Recurrent Optical Breakdown," *Physics-Doklady*, Vol. 41, No. 11, 1996, pp. 566–567.

[14] Sakai, T., "Supersonic Drag Performance of Truncated Cones with Repetitive Energy Depositions," *International Journal of Aerospace Innovations*, Vol. 1, No. 1, 2009, pp. 31–43. doi:10.1260/175722509787549471

[15] Sasoh, A., Ohtani, T., and Mori, K., "Pressure Effects in a Shock-Wave-Plasma Interaction Induced by a Focused Laser Pulse," *Physical Review Letters*, Vol. 97, No. 20, Nov. 2006, p. 205004.

K. Asai
Associate Editor